Gateway to all-optical spin switching in Heusler ferrimagnets: Pancharatnam-Berry tensor and magnetic moment ratio

G. P. Zhang [*]
Department of Physics, Indiana State University, Terre Haute, Indiana 47809, USA

Y. Q. Liu and M. S. Si
School of Materials and Energy, Lanzhou University, Lanzhou 730000, China

Nicholas Allbritton
Department of Physics, Indiana State University, Terre Haute, Indiana 47809, USA

Y. H. Bai
Office of Information Technology, Indiana State University, Terre Haute, Indiana 47809, USA

Wolfgang Hübner
Department of Physics, Rheinland-Pfälzische Technische Universität, Kaiserslautern-Landau, 67653 Kaiserslautern, Germany

Thomas F. George
*Departments of Chemistry & Biochemistry and Physics & Astronomy,
University of Missouri - St. Louis, St. Louis, Missouri 63121, USA*

All-optical spin switching (AOS) is a new phenomenon found in a small group of magnetic media, where a single laser pulse can switch spins from one direction to another, without assistance of a magnetic field, on a time scale much shorter than existing magnetic technology. However, despite intensive efforts over a decade, its underlying working principle remains elusive. Here through manganese-based Heusler ferrimagnets, we show that a group of flat bands around the Fermi level act as gateway states to form efficient channels for spin switching, where their noncentrosymmetry allows us to correlate the spin dynamics to the second-order optical response. To quantify their efficacy, we introduce the third-rank Pancharatnam-Berry tensor (PB tensor), $\boldsymbol{\eta}^{(3)} = \langle i|\mathbf{p}|m\rangle\langle m|\mathbf{p}|f\rangle\langle f|\mathbf{p}|i\rangle$, where $|i\rangle$, $|m\rangle$ and $|f\rangle$ are initial, intermediate and final band states, respectively, and $\mathbf{p}$ is the momentum operator. A picture emerges: Those which show AOS, such as the recently discovered Mn_2RuGa, always have a large PB tensor element but have a small sublattice spin moment ratio, consistent with the prior experimental small remanence criterion. This does not only reveal that the delicate balance between the large PB tensor element and the small sublattice spin ratio plays a decisive role in AOS, but also, conceptually, connects the nth-order nonlinear optics to $(n + 1)$th-rank PB tensors in general.

Introduction. For over half a century, magnetic storage technology has relied on a magnetic field to switch magnetization in magnetic drives. Beaurepaire and coworkers [1] changed this picture by showing that a femtosecond laser pulse can directly demagnetize the magnetic nickel film within 1 ps, representing the beginning of femtomagnetism [2]. In 2007, Stanciu and coworkers [3] reported that a single laser pulse alone, without assistance of a magnetic field, is able to switch spins from one direction to another in GdFeCo, called all-optical spin switching (AOS). Subsequent investigations [4–11] soon discovered a large group of AOS materials [5,6,12–14]. It has been shown that whether or not AOS occurs sensitively depends on the sample composition [13,15], thickness [16,17], remanence [18], number of laser pulses, laser fluences, and other parameters [15] (see recent reviews for details [7,19]). Mentink *et al.* [20] suggested an intersite spin exchange model for AOS. Recently Jakobs and Atxitia [21] proposed a criterion based on a transition from a relativistic relaxation path to an exchange-dominated regime.

Unfortunately, most AOS materials are amorphous, which significantly limits access to their microscopic electronic and magnetic structures, beyond the classical atomistic spin model level [15,22]. Although crystalline AOS materials are also discovered [14,23,24], they often need multiple laser pulses to switch spins [12,25], thus not ideal for future applications. Heusler alloys are different [26–39]. They are crystalline and more importantly their electronic and magnetic properties can be systematically tuned [40] without a significant change to their structures. What is even more interesting is that one of the Heusler compounds, Mn_2RuGa, shows single-pulse

_____
[*]guo-ping.zhang@outlook.com

all-optical spin switching [41]. This presents a rare opportunity for a first-principles investigation, beyond earlier model simulations [21,42,43].

In this Letter, we employ four manganese-based non-centrosymmetric Heuslers Mn_2YZ and the time-dependent first-principles method to pin down two critical elements that underline the all-optical spin switching. First, a group of flat bands, a few eV around the Fermi level, act as gateway states for spin switching. To quantify the efficacy of these states, we introduce the Pancharatnam-Berry (PB) tensor, a geometric tensor that consists of a product of momentum matrix elements between transition states. Channels involving flat bands have a large PB tensor element, found across all the four Heuslers. Second, the spin moment ratio between two Mn sublattices must be small. This is only found in Mn_2RuGa and Mn_2RuAl, not in Mn_2IrGa and Mn_2RuGe. Our finding conceptually establishes the link between the $(n+1)$th PB tensor to the nth-order optical process, and reveals that it is the balance between a large PB tensor element and a small spin moment ratio that leads to all-optical spin switching. Our finding will have a profound impact on the future direction of the experimental and theoretical research, by focusing on crystalline Heuslers. In particular, since all four materials investigated here are already available, this will motivate an immediate experimental investigation.

Correlation between the spin and charge dynamics and Pancharatnam-Berry momentum tensor. AOS is an optical process. What is probed often differs from what one wishes to probe, similar to time-resolved magnetooptics [44]. Figure 1(a) schematically illustrates a laser pulse impinging on a sample, where one detects the polarization change and derives the spin change from it. Theoretically, we first solve the Kohn-Sham equation for the ground-state properties [45],

$$\left[-\frac{\hbar^2 \nabla^2}{2m_e} + V_{Ne} + V_H + V_{xc}\right]\psi_{n\mathbf{k}}(\mathbf{r}) = E_{n\mathbf{k}}\psi_{n\mathbf{k}}(\mathbf{r}), \quad (1)$$

where $\psi_{n\mathbf{k}}(\mathbf{r})$ is the wave function of band n at the crystal momentum $\mathbf{k}$, and $E_{n\mathbf{k}}$ is its band energy. The terms on the left are the kinetic energy operator, the attraction between the nuclei and electrons, the Hartree term, and the exchange-correlation, respectively. The spin-orbit coupling (SOC) is included using a second-variational method in the same self-consistent iteration. We describe the optical interaction with a matter by the time-dependent Liouville equation [44,46] (additional details can be found in the Supplemental Material (SM) [47]),

$$\frac{d\rho}{dt} = \frac{1}{i\hbar}[H_0 + H_I, \rho], \quad (2)$$

where ρ is the density matrix, H_0 is the unperturbed system Hamiltonian and H_I is the interaction between the laser field and the system [47]. The Liouville equation builds in the Pauli exclusion principle, can be extended to many-body states, and works well with other software such as VASP, QUANTUM ESPRESSO, and ELK. The nth-order density matrix is given by [48]

$$\rho^{(n)}(t) = (i\hbar)^{-n}U_0(t)\int_{-\infty}^{t}dt_1\int_{-\infty}^{t_1}dt_2\cdots\int_{-\infty}^{t_{n-1}}dt_n[H_I(t_1),$$

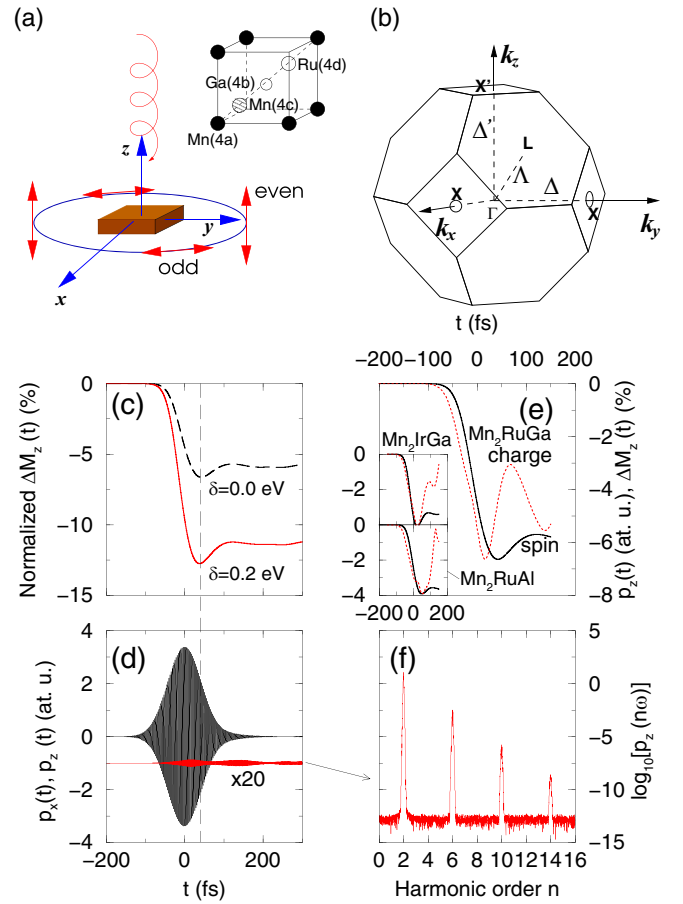$$\{H_I(t_2),\cdots[H_I(t_n),\rho_0]\cdots]\}U_0(-t), \quad (3)$$

FIG. 1. (a) Schematic of the interaction between a σ pulse and Mn_2RuGa. Even and odd harmonics are emitted along two different directions. Inset: Simplified crystal structure of Mn_2RuGa, where the filled circles are Mn_{4a}, and the shaded circle is Mn_{4c}, the small and large empty circles are the Ga_{4b} and Ru_{4d} atoms, respectively. (b) The Brillouin zone of Mn_2RuGa. (c) Spin change $\Delta M_z = \left(\frac{M_z(t)}{M_z(-\infty)} - 1\right)$ for two intraband cutoffs $\delta = 0.0$ (dashed line) and 0.2 eV (solid line). (d) p_x and p_z as a function of time. (e) Envelope of p_z (red dotted lines) and ΔM_z (solid lines) changes with time for Mn_2RuGa, Mn_2IrGa, and Mn_2RuAl (insets). (f) Logarithmic harmonic signals along the z axis.

where $U_0(t) = \exp(-iH_0t/\hbar)$. The symmetry property of electron and spin dynamics is encoded in the expectation value of an operator. For the reason that will become clear below, we take the second-order momentum $\langle\mathbf{p}\rangle^{(2)}(t) = \text{Tr}[\mathbf{p}\rho^{(2)}(t)]$ as an example. Under a symmetry operation $\{R\}$, $\langle\mathbf{p}\rangle^{(2)}(t)$ transforms as a tensor (in the component form)

$$\langle p\rangle_{lmn}^{(2)}(t) = \sum_{abc}R_{la}R_{mb}R_{nc}\langle p\rangle_{abc}^{(2)}(t), \quad (4)$$

where l and a are the new and old Cartesian indices of $\mathbf{p}$, respectively, and the index pairs (bc) and (mn) are Cartesian indices of two laser fields before and after symmetry transformation. The entire procedure is exactly the same as the transformation between two susceptibility tensors $\chi^{(2)}$ and $\chi^{(2)'}$ in nonlinear optics as [48] $\chi_{lmn}^{(2)'} = \sum_{abc}R_{la}R_{mb}R_{nc}\chi_{abc}^{(2)}$.

The situation of spin is different. Spin is an axial vector and transforms under the SU(2) symmetry [49,50]. For

the same second-order response, the spin expectation value, $\langle \mathbf{s} \rangle^{(2)}(t) = \text{Tr}[\mathbf{s}\rho^{(2)}(t)]$, transforms as in a similar fashion as the Hall effect [51]

$$\langle s \rangle^{(2)}_{lmn}(t) = \sum_{abc} R_{la}R_{mb}R^s_{nc} \langle s \rangle^{(2)}_{abc}(t), \tag{5}$$

where the transformation matrix for spin R^s_{nc} is given as $R^s_{nc} = |R|R_{nc}$ and $|R|$ is its determinant [49]. The second-order response in Eq. (5) is the lowest-order response of the spin, and the first order is zero because the product of one axial and one polar vector is zero [49], except that the axial and polar vectors are collinear and the symmetry is low. Because $\rho^{(2)}(t)$ is proportional to the square of the laser field, that is why the (de)magnetization is linearly proportional to the laser fluence as observed in experiments [52,53] before saturation, and it is also the reason why we choose the second-order density matrix above. Regardless of whether the system has inversion symmetry or not, all even orders of the spin, including the zeroth order, survive. However, for the momentum, if the system has inversion symmetry, the multiplication of three R's yields $(-1)(-1)(-1) = -1$ and it cancels out all even orders, including the second order here. Only odd orders survive. Therefore, in order to detect spin dynamics through the charge dynamics or more precisely the optical response, at minimum one must choose a system without inversion symmetry, so the second-order $\langle \mathbf{p}^{(2)} \rangle$ and $\langle \mathbf{s}^{(2)} \rangle$ share the same field dependence such as $H_I(t_1)H_I(t_2)$. If a system has inversion symmetry, then there is a mismatch between spin and charge responses. For a transition through a channel $|i\rangle \rightarrow |m\rangle \rightarrow |f\rangle \rightarrow |i\rangle$, the expectation value of the momentum $\langle \mathbf{p} \rangle^{(2)}(t)$ is related to the tensor

$$\boldsymbol{\eta}^{(3)}(C) = \langle i|\mathbf{p}|m\rangle\langle m|\mathbf{p}|f\rangle\langle f|\mathbf{p}|i\rangle, \tag{6}$$

which is very similar to the Pancharatnam-Berry phase [54,55] for discrete paths [56], $\gamma(C) = -\text{Im} \ln [\langle\phi_1|\phi_2\rangle\langle\phi_2|\phi_3\rangle\cdots\langle\phi_{N-1}|\phi_N\rangle]$. Here $\{\phi_i\}$ are N number of nonorthogonal states and C refers to the close path in the functional space. We call $\boldsymbol{\eta}^{(3)}(C)$ the third-order Pancharatnam-Berry momentum tensor (PB tensor). It obeys the sum rule as

$$\sum_{mf}(E_i - E_m)(E_m - E_f)(E_f - E_i)\boldsymbol{\eta}^{(3)}(C) = \langle i|[H,\mathbf{p}]^3|i\rangle, \tag{7}$$

which is zero for a system with inversion symmetry. This connects the experimental detectables to those undetectable, which forms the basis of our study [47].

Results. Mn$_2$RuGa has a space group symmetry of F$\bar{4}$3m, with no inversion symmetry. Figure 1(a) is a simplified version of the structure, where one Mn is situated at the 4a site (filled circle) and another Mn at the 4c site (shaded circles). Ru and Ga take the 4d and 4b sites (small and large empty circles), respectively. Without SOC, only one term $\langle p \rangle^{(2)}_{3,1,2}(t)$ is independent, where (312) are cyclic Cartesian indices. With SOC, there are three, and we choose $\langle p \rangle^{(2)}_{3,1,2}(t)$, so even-order signals polarize along the z axis and are spatially separated from odd orders whose polarization is along the x and y axes. Figure 1(a) illustrates this process, where the light propagates along the $-z$ axis with its vector potential in the xy plane, $\mathbf{A}(t) = A_0 \exp(-t^2/\tau^2)(\cos\omega t\hat{x} \pm \sin\omega t\hat{y})$. Here A_0 is

the amplitude, τ is the laser pulse duration, t is the time, and $\hat{x}$ and $\hat{y}$ are the unit vectors of the x and y axes, respectively. In the presence of SOC, we include all the valence states from -0.4124 Ry up to the Fermi energy of 0.662 Ry, as well as the partially and completely unoccupied states up to 2.156 Ry. In total, there are 76 states at each $\mathbf{k}$ point. Semicore and core states are not included, since they appear below -2.37 Ry. Including more states produces no visible effect. We use an extremely dense $\mathbf{k}$ mesh of $48\times48\times48$ for all the results here, while the test of $\mathbf{k}$ convergence is given in the SM [47]. Figure 1(c) shows ultrafast demagnetization (long dashed line) under a laser pulse of $\tau = 60$ fs, $\hbar\omega = 1.6$ eV, and $A_0 = 0.015$ Vfs/Å. So the fluence is 1.33 mJ/cm^2. Including the intraband transition (the red line with $\delta = 0.2$ eV) [46,47] bolsters the demagnetization from 7%–13%, consistent with the experimental findings [57]. $\Delta M_z(t)$ is very smooth without rapid oscillation. By contrast, the charge response, i.e., $p_x(t)$ and $p_z(t)$, beats strongly. Figure 1(d) illustrates that $p_x(t)$ closely follows the laser field and peaks at 0 fs, which is ahead of the spin by 40 fs. The vertical line across Figs. 1(c) and 1(d) highlights this delay of the spin with respect to the charge response [58]. $p_z(t)$ is much weaker and does not peak at 0 fs. We magnify p_z by 20 times and then vertically shift it down by one unit. Since p_z still has rapid oscillations, we take its negative envelope and superimpose it on the spin change in Fig. 1(e) (see the solid line). We find that the leading edge of $p_z(t)$ (dashed line) matches that of $\Delta M_z(t)$, far better than $p_x(t)$. We have tested three additional Heuslers, Mn$_2$RuAl, Mn$_2$IrGa, and Mn$_2$RuGe. We find that only Mn$_2$RuGe has a stronger deviation (see Ref. [47]), and the rest show a consistent match between $p_z(t)$ and $\Delta M_z(t)$ (see two insets for Mn$_2$RuAl and Mn$_2$IrGa). This demonstrates that our numerical result confirms our above analysis. This match is important as it allows us to use $p_z(t)$ to understand $\Delta M_z(t)$. Obviously, a perfect match is not expected.

We Fourier transform $p_z(t)$ into the frequency domain [Fig. 1(f)], where the second order dominates, and then disperse it along the Γ-X direction [Fig. 1(b)]. Figure 2(a) shows such a plot for the spin majority channel under σ^+ excitation. We notice that most $\mathbf{k}$ points along the Γ-X direction have a weak harmonic signal. The strongest one is at $(\frac{44}{48}, 0, 0)\frac{2\pi}{a}$, close to the X point, where a is the lattice constant. In Fig. 2(b), we show the band structure for the majority band, where we draw a dashed line vertically across Figs. 2(a) and 2(b) to pinpoint which bands are involved in harmonic generation. Our Fermi energy without SOC is at $E_F = 0.652$ Ry. We number our band states from Ga's 3p states at $E_{3p}(\text{Ga}) = -6.252$ Ry, i.e., from 1–3. States 4 and 5 are Mn's 3s states at $E_{3s}(\text{Mn}_{4c}) = -5.288$ Ry and $E_{3s}(\text{Mn}_{4a}) = -5.08$ Ry. State 6 is Ru's 5s state at $E_{5s}(\text{Ru}) = -4.67$ Ry, followed by six Mn's 3p states from 7–12 at $E_{3p}(\text{Mn}_{4c}) = -2.990$ and $E_{3p}(\text{Mn}_{4a}) = -2.466$ Ry, respectively. Finally, states 13–15 are Ru's 5p state at $E_{5p}(\text{Ru}) = -2.466$ Ry. The valence bands start from band 16 at -0.403 Ry. Figure 2(b) only shows bands from $|29\rangle$ to $|38\rangle$. A particular challenge in Mn$_2$RuGa is that bands are strongly hybridized, so it is rather cumbersome to denote them by their orbital characters. Table I shows that $|29\rangle$ and $|30\rangle$ are a hybridized band formed by Mn$_{4a}$-3d, Mn$_{4c}$-3d, Ru-4d, and Ga-4p states, while $|38\rangle$ is dominated by Mn$_{4c}$-3d and Ru-4d. A detailed discussion is given in
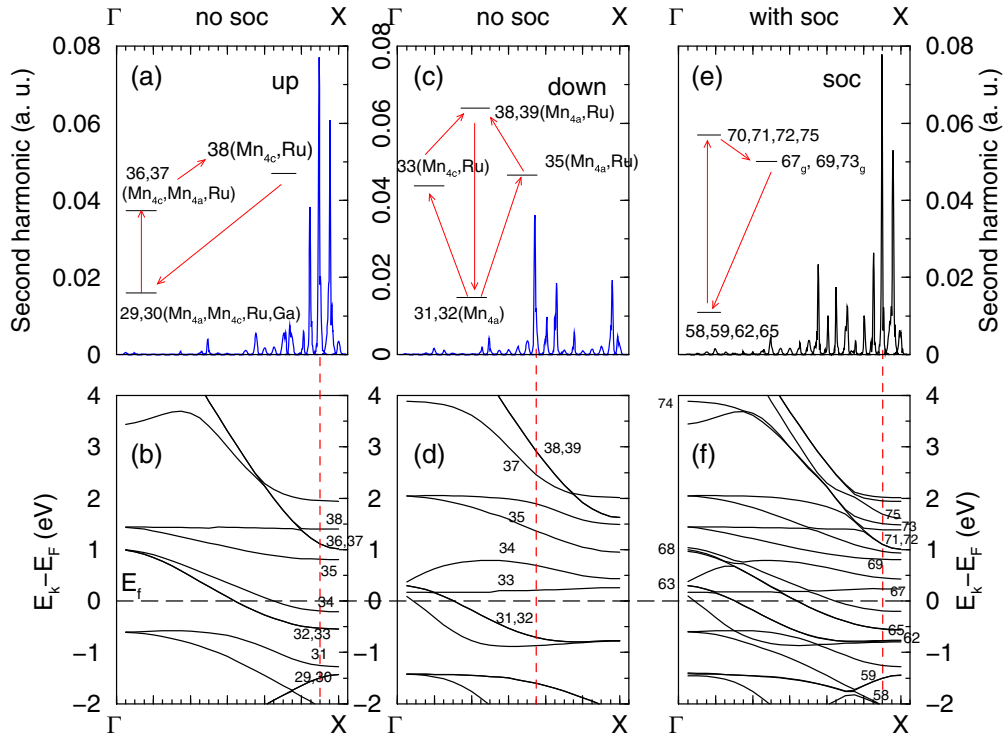
FIG. 2. (a) Second harmonic signal of the spin majority channel dispersed along the Γ-X direction, without spin-orbit coupling. The vertical one denotes the location of the largest peak at $(\frac{44}{48}, 0, 0)\frac{2\pi}{a}$. (b) Band structure of the spin majority channel, where the horizontal dashed line is the Fermi level. (c) The same as (a), but for the spin minority channel, where the maximum peak is shifted to $(\frac{30}{48}, 0, 0)\frac{2\pi}{a}$. (d) Spin minority band structure. (e) Second harmonic signal with spin-orbit coupling, whose maximum peak is shifted back to $(\frac{44}{48}, 0, 0)\frac{2\pi}{a}$. The numbers with subscript *g* refer to the flat band gateway states. (f) Band structure with SOC.

Table II of SM [47]. Figure 2(c) shows the second harmonic from the spin minority channel. Because the minority channel has nearly zero density of states (DOS) at the Fermi level [39,59], this cuts off signals significantly. Its maximum is only half the majority channel and is shifted to a different point, $(\frac{30}{48}, 0, 0)\frac{2\pi}{a}$.

The PB tensor $\eta^{(3)}(\mathbf{k})$ has three band indices, i, m, and f, for each transition channel, written as $|i\rangle \rightarrow |m\rangle \rightarrow |f\rangle \rightarrow |i\rangle$. Most channels have a small element. We

disperse the largest elements along the Γ-X direction (Δ line) in Fig. 3(a). At Γ, we find the first dominant channel is $|43\rangle \rightarrow |74\rangle \rightarrow |63\rangle \rightarrow |43\rangle$ (see the circles), where bands $|74\rangle$ and $|63\rangle$ are shown in Fig. 2(f) but $|43\rangle$ is not because its energy is too low. As we move away from Γ, channel $|43\rangle \rightarrow |74\rangle \rightarrow |63\rangle \rightarrow |43\rangle$ smoothly transitions to $|44\rangle \rightarrow |74\rangle \rightarrow |63\rangle \rightarrow |43\rangle$. Once we encounter a band crossing, $\eta^{(3)}(\mathbf{k})$ suddenly changes (see the squares and diamonds). Whenever there is no crossing, a smooth change

TABLE I. (Top) Composition of the majority band states at $(\frac{44}{48}, 0, 0)\frac{2\pi}{a}$ and (bottom) that of the minority band states at $(\frac{30}{48}, 0, 0)\frac{2\pi}{a}$. The band indices are shown in Fig. 2. *l* refers to the orbital angular momentum quantum number. The numbers given under each column are partial charges in percentages. Since the majority and minority states are from different **k**, one should not add them up.

| Majority states	Mn$_{4a}$			Mn$_{4c}$			Ru			Ga		
$(\frac{44}{48}, 0, 0)\frac{2\pi}{a}$	$l=0$	$l=1$	$l=2$	$l=0$	$l=1$	$l=2$	$l=0$	$l=1$	$l=2$	$l=0$	$l=1$	$l=2$
$|29\rangle, |30\rangle$	0	3.71	13.88	0	5.78	8.92	0	6.41	10.57	0	18.25	0.01
$|36\rangle, |37\rangle$	0	1.15	18.46	0	0.82	59.52	0	0.98	10.48	0	0.57	1.42
$|38\rangle$	0	0	0	0	0	71.85	0	0	25.84	0	0	0
Minority states	Mn$_{4a}$			Mn$_{4c}$			Ru			Ga		
$(\frac{30}{48}, 0, 0)\frac{2\pi}{a}$	$l=0$	$l=1$	$l=2$	$l=0$	$l=1$	$l=2$	$l=0$	$l=1$	$l=2$	$l=0$	$l=1$	$l=2$
$|31\rangle, |32\rangle$	0	2.50	45.29	0	8.33	0.67	0	5.72	3.78	0	7.68	0.58
$|33\rangle$	0	0	4.57	0	0	51.60	0	0	40.00	0	0	0.15
$|35\rangle$	0	0	78.75	0	0	0.01	0	0	11.45	0	0	0.69
$|38\rangle, |39\rangle$	0	3.87	42.54	0	3.92	8.67	0	3.37	16.46	0	4.51	1.31
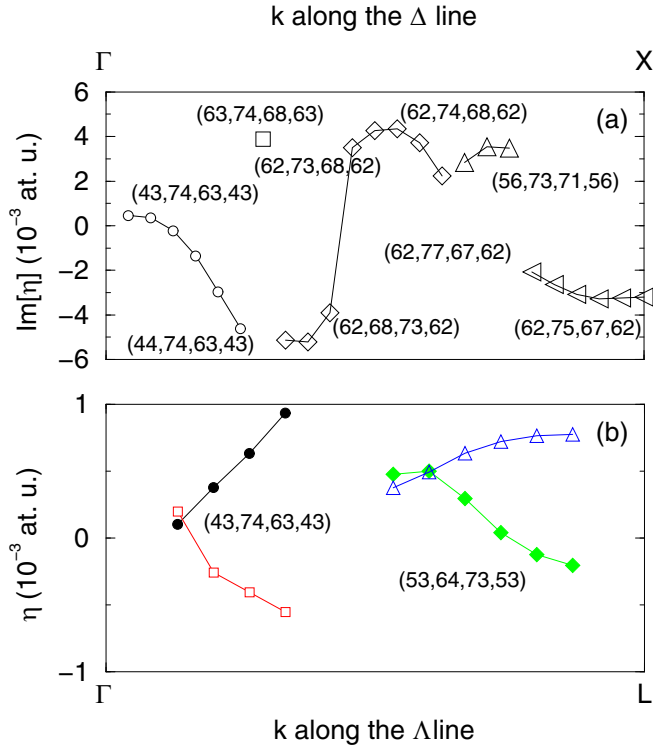
FIG. 3. (a) Large elements of the Pancharatnam-Berry tensor $\eta^{(3)}(\mathbf{k})$ in units of $\hbar^3/a_0^3$ along the Γ-X direction for a few selected channels denoted by (i, m, f, i) in the figure, same as $|i\rangle \rightarrow |m\rangle \rightarrow |f\rangle \rightarrow |i\rangle$ in the main text, where band indices i, m, f are those bands shown in Fig. 2(f). We link symbols by lines only if they have similar channel states. For instance, the circles are mainly due to $|43\rangle \rightarrow |74\rangle \rightarrow |63\rangle \rightarrow |43\rangle$. All the elements are all imaginary. (b) Pancharatnam-Berry tensor $\eta^{(3)}(\mathbf{k})$ elements along the Γ-L direction, which is much weaker. The filled symbols are the real part of $\eta^{(3)}(\mathbf{k})$, while the unfilled symbols are the imaginary part of $\eta^{(3)}(\mathbf{k})$.

is found from one $\mathbf{k}$ to another. This further confirms that the PB tensor is well defined [47]. A much smaller tensor element is found along the Γ-L line (Λ line), because two flat bands are absent along this direction [39,60,61], where $\eta^{(3)}(\mathbf{k})$ is below our numerical uncertainty limit. Because of multiple band crossings, we only find two regions with a smooth dispersion. One is between $(\frac{1}{48}, \frac{1}{48}, -\frac{1}{48})\frac{2\pi}{a}$ and $(\frac{5}{48}, \frac{5}{48}, -\frac{5}{48})\frac{2\pi}{a}$, and the other is between $(\frac{8}{48}, \frac{8}{48}, -\frac{8}{48})\frac{2\pi}{a}$ and $(\frac{13}{48}, \frac{13}{48}, -\frac{13}{48})\frac{2\pi}{a}$. Different from the Γ-X line, $\eta^{(3)}(\mathbf{k})$ has both real (filled symbols) and imaginary parts (empty symbols). In summary, we have six channels: four for the minority, $|31\rangle \substack{\nearrow |33\rangle \rightarrow |38\rangle \searrow \\ \searrow |35\rangle \rightarrow |38\rangle \nearrow} |31\rangle$, $|32\rangle \substack{\nearrow |33\rangle \rightarrow |39\rangle \searrow \\ \searrow |35\rangle \rightarrow |39\rangle \nearrow} |32\rangle$, where the band indices are shown in Fig. 2(d), and two for the majority, $|29\rangle \rightarrow |36\rangle \rightarrow |38\rangle \rightarrow |29\rangle$, $|30\rangle \rightarrow |37\rangle \rightarrow |38\rangle \rightarrow |30\rangle$, where indices are shown in Fig. 2(b). Figure 2(b) reveals that the flat band $|38\rangle$ is at the center of the majority channel excitation. We call it a gateway state. The gateway state in the minority channel is $|33\rangle$, which is also a flat band [see Fig. 2(d)]. Including SOC does not change the picture, except that the harmonic maximum shifts back to $(\frac{44}{48}, 0, 0)\frac{2\pi}{a}$ [Fig. 2(e)] and the flat bands are renumbered due to the doubling number of bands [Fig. 2(f)]. They are now $|67\rangle$ and $|73\rangle$.

Are these flat bands essential to AOS? We employ three additional Heuslers, Mn_2YZ, where Y is Ir [62] and Z is Ge and Al [28,63]. Figures 4(a) and 4(b) show that Mn_2RuGe has two similar flat bands, but its Fermi level is raised clearly with respect to Mn_2RuGa [compare with Figs. 4(c) and 4(d)]. Replacing Ga by Al has the smallest effect on the band structure among all three new Heuslers [see Figs. 4(e) and 4(f)]. The flat bands are retained. When we replace Ru by Ir [62], the flat band in the majority is lowered, and that in the minority is now at the Fermi level, which explains why it has a giant coercivity [62].

We recall that in GdFeCo and TbFe the spin moment ratios of two spin sublattices are always very close to each other [64]. We compute the ratio between the spin moment on Mn_{4a} and Mn_{4c}. The results are shown in Fig. 4(i). To our surprise, there is a significant variation. Mn_2RuGa and Mn_2RuAl have the smallest ratio, while Mn_2RuGe and Mn_2IrGa have a larger ratio. The smaller ratio between two spin sublattices is consistent with the small remanence criteria [18] proposed much earlier. Figure 4(j) reveals the optical requirement of AOS through the PB tensor $\eta^{(3)}(\mathbf{k})$. We see that Mn_2RuGe has the strongest value and Mn_2RuGa has the smaller value. Because a strong optical excitation and a strong magnetic excitation are always opposite to each other, it is likely that the competition between these two underlines the all-optical spin switching.

Connection to future experiments. An experimental test of our theoretical prediction is exactly what we had in mind when we carried out this study. For this reason, all the Heusler compounds, Mn_2RuAl, Mn_2RuSn, Mn_2RuSi, Mn_2RuGa, Mn_2IrGa, and Mn_2RuGe, are already synthesized experimentally or well studied theoretically. The lattice constant a of Mn_2RuGa, 5.97 Å, matches that of GaAs, 5.75 Å, within 3.6%, very attractive integration of a semimetal into a state-of-the-art semiconductor, to extend the boundary of spintronics.

We have three suggestions for experimentalists. First, since Mn_2RuAl has similar electronic, magnetic, and optical properties as Mn_2RuGa, we would expect that the chance to observe AOS in Mn_2RuAl is high. So an experimental test of AOS on Mn_2RuAl will test our first prediction.

Second, Mn_2RuGe differs from Mn_2RuGa by an extra electron in the outer shell. Mn_2RuGe has the largest spin ratio among all four Heuslers investigated. We do not expect a single pulse AOS in this system. Whether or not AOS occurs in Mn_2RuGe will directly test our magnetic moment ratio prediction.

Third, Mn_2IrGa presents another opportunity. Here Ir (in Mn_2IrGa) and Gd (in GdFeCo) both have $4f$ and $5d$ shells. Although Gd is different from Ru and Ir, Gd is the only one among $4f$ rare-earth elements that has $5d$ electrons and is thus similar to Ru and Ir, whereas $4f$ electrons play a minor role as demonstrated in magnetic anisotropy [65]. Ir's $4f$ shell is completely filled, since its native electron configuration is $Xe4f^{14}5d^76s^2$. $4f$ in Gd is half filled since its configuration is $Xe4f^75d6s^2$. They both have zero orbital moment from the $4f$ shell. In addition, Ir also has zero spin moment from the $4f$ shell. Whether AOS in Mn_2IrGa occurs experimentally allows one to distinguish the role of $4f$, with respect to their
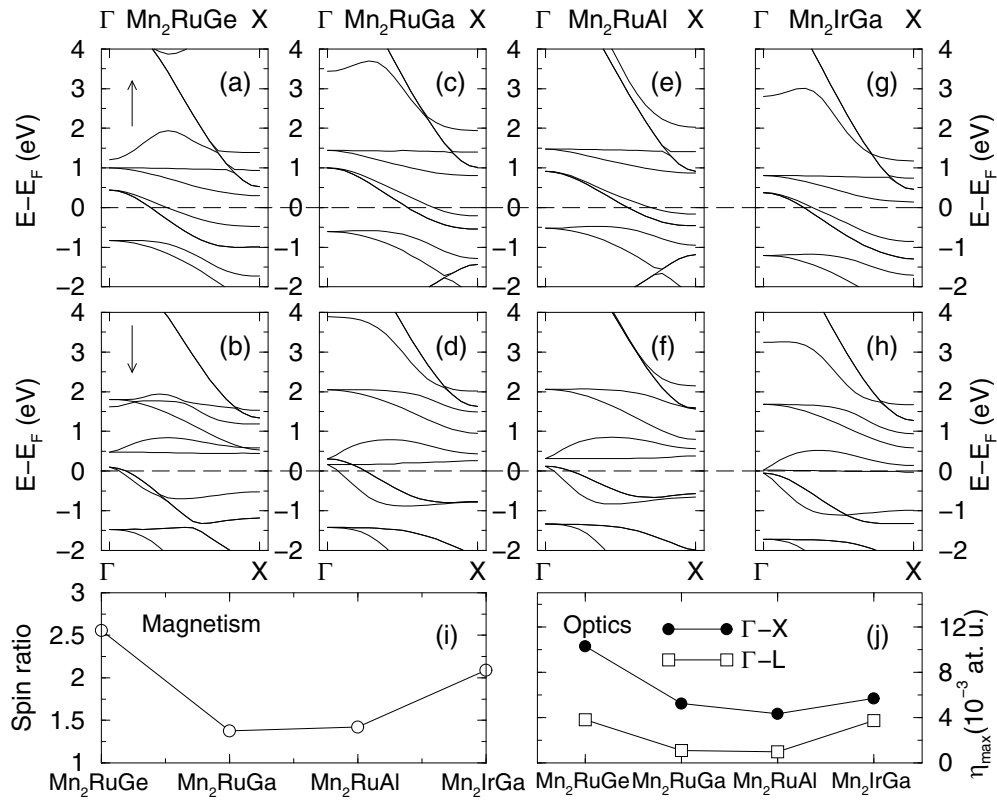
FIG. 4. (a)–(h) Comprehensive band structure comparison among four Heusler compounds, Mn_2RuGe, Mn_2RuGa, Mn_2RuAl, and Mn_2IrGa. The majority bands are in (a), (c), (e), and (g), while the minority are in (b), (d), (f), and (h). (i) Spin moment ratio between two Mn atoms. (j) Maximum PB tensor elements $\eta^{(3)}(\mathbf{k})$ along the Γ-X and Γ-L directions.

differences in $5d$. Since Ru's native electron configuration is $Kr4d^75s^1$, a comparison between Mn_2IrGa and Mn_2RuGa is potentially able to compare and contrast the roles of $4d$ and $5d$ in AOS. Therefore, we believe there are ample opportunities that await experimental verifications.

In conclusion, we have shown that a group of flat bands, with a large PB tensor, act as gateway states that channel one sublattice spin to another to realize all-optical spin switching in Mn-based Heusler ferrimagnets. This is the origin of the theoretical intersite exchange model by Mentink *et al.* [20]. Although all four Heuslers have flat bands, only Mn_2RuGa and Mn_2RuAl have a small spin moment ratio between two spin sublattices, explaining the experimental low remanence criterion [18]. Our finding will have a significant impact on future research on two fronts. Conceptually, the Pancharatnam-Berry tensor extends the Berry phase [55] and connects the nth-order nonlinear optics to the $(n + 1)$th PB tensor, so one has a way to quantify the efficacy of nonlinear optical ma-

terials. More importantly, since all four Heuslers are readily available, their supertunability renders them an ideal test bed, representing a paradigm shift for future experimental and theoretical investigations of all-optical spin switching.

Note added. Recently, two papers proposed a similar tensor based on the triplet products of the dipoles, not for the momenta as done here [66,67].

[1] E. Beaurepaire, J. C. Merle, A. Daunois, and J.-Y. Bigot, Ultrafast spin dynamics in ferromagnetic nickel, Phys. Rev. Lett. **76**, 4250 (1996).

[2] G. P. Zhang, W. Hübner, E. Beaurepaire, and J.-Y. Bigot, Laser-induced ultrafast demagnetization: Femtomagnetism, A new frontier? Topics Appl. Phys. **83**, 245 (2002).

[3] C. D. Stanciu, F. Hansteen, A. V. Kimel, A. Kirilyuk, A. Tsukamoto, A. Itoh, and T. Rasing, All-optical magnetic recording with circularly polarized light, Phys. Rev. Lett. **99**, 047601 (2007).

[4] T. A. Ostler, J. Barker, R. F. L. Evans, R. W. Chantrell, U. Atxitia, O. Chubykalo-Fesenko, S. El Moussaoui Moussaoui,

L. Le Guyader, E. Mengotti, L. J. Heyderman, F. Nolting, A. Tsukamoto, A. Itoh, D. Afanasiev, B. A. Ivanov, A. M. Kalashnikova, K. Vahaplar, J. Mentink, A. Kirilyuk, Th. Rasing, and A. V. Kimel, Ultrafast heating as a sufficient stimulus for magnetization reversal in a ferrimagnet, Nat. Commun. **3**, 666 (2012).

[5] S. Mangin, M. Gottwald, C.-H. Lambert, D. Steil, V. Uhlir, L. Pang, M. Hehn, S. Alebrand, M. Cinchetti, G. Malinowski, Y. Fainman, M. Aeschlimann, and E. E. Fullerton, Engineered materials for all-optical helicity-dependent magnetic switching, Nat. Mater. **13**, 286 (2014).

[6] C.-H. Lambert, S. Mangin, B. S. D. Ch. S. Varaprasad, Y. K. Takahashi, M. Hehn, M. Cinchetti, G. Malinowski, K. Hono, Y. Fainman, M. Aeschlimann, and E. E. Fullerton, All-optical control of ferromagnetic thin films and nanostructures, Science **345**, 1337 (2014).

[7] G. P. Zhang, M. Murakami, M. S. Si, Y. H. Bai, and T. F. George, Understanding all-optical spin switching: Comparison between experiment and theory, Mod. Phys. Lett. B **32**, 1830003 (2018).

[8] Y. Quessab, M. Deb, J. Gorchon, M. Hehn, G. Malinowski, and S. Mangin, Resolving the role of magnetic circular dichroism in multishot helicity-dependent all-optical switching, Phys. Rev. B **100**, 024425 (2019).

[9] J.-X. Lin, M. Hehn, T. Hauet, Y. Peng, J. Igarashi, Y. Le Guen, Q. Remy, J. Gorchon, G. Malinowski, S. Mangin, and J. Hohlfeld, Single laser pulse induced magnetization switching in in-plane magnetized GdCo alloys, Phys. Rev. B **108**, L220403 (2023).

[10] J. Wang, M. Li, C. Li, R. Tang, M. S. Si, G. Chai, J. Yao, C. Jia, and C. Jiang, Piezostrain-controlled magnetization compensation temperature in ferrimagnetic GdFeCo alloy films, Phys. Rev. B **107**, 184424 (2023).

[11] Y. Kasatani, H. Yoshikawa, and A. Tsukamoto, Electrical detection and current control of all-optical magnetization switching in GdFeCo ferrimagnetic alloy thin film, Jpn. J. Appl. Phys. **62**, SB1014 (2023).

[12] S. Alebrand, M. Gottwald, M. Hehn, D. Steil, M. Cinchetti, D. Lacour, E. E. Fullerton, M. Aeschlimann, and S. Mangin, Light-induced magnetization reversal of high-anisotropy TbCo alloy films, Appl. Phys. Lett. **101**, 162408 (2012).

[13] A. Hassdenteufel, B. Hebler, C. Schubert, A. Liebig, M. Teich, M. Helm, M. Aeschlimann, M. Albrecht, and R. Bratschitsch, Thermally assisted all-optical helicity dependent magnetic switching in amorphous $Fe_{100-x}Tb_x$ alloy films, Adv. Mater. **25**, 3122 (2013).

[14] M. Vomir, M. Albrecht, and J.-Y. Bigot, Single shot all optical switching of intrinsic micron size magnetic domains of a Pt/Co/Pt ferromagnetic stack, Appl. Phys. Lett. **111**, 242404 (2017).

[15] K. Vahaplar, A. M. Kalashnikova, A. V. Kimel, S. Gerlach, D. Hinzke, U. Nowak, R. Chantrell, A. Tsukamoto, A. Itoh, A. Kirilyuk, and T. Rasing, All-optical magnetization reversal by circularly polarized laser pulses: Experiment and multiscale modeling, Phys. Rev. B **85**, 104402 (2012).

[16] B. Hebler, A. Hassdenteufel, P. Reinhardt, H. Karl, and M. Albrecht, Ferrimagnetic Tb-Fe alloy thin films: Composition and thickness dependence of magnetic properties and all-optical switching, Front. Mater. **3**, 8 (2016).

[17] J. Gorchon, C.-H. Lambert, Y. Yang, A. Pattabi, R. B. Wilson, S. Salahuddin, and J. Bokor, Single shot ultrafast all optical magnetization switching of ferromagnetic Co/Pt multilayers, Appl. Phys. Lett. **111**, 042401 (2017).

[18] A. Hassdenteufel, J. Schmidt, C. Schubert, B. Hebler, M. Helm, M. Albrecht, and R. Bratschitsch, Low-remanence criterion for helicity-dependent all-optical magnetic switching in ferrimagnets, Phys. Rev. B **91**, 104431 (2015).

[19] P. Scheid, Q. Remy, S. Lebegue, G. Malinowski, and S. Mangin, Light induced ultrafast magnetization dynamics in metallic compounds, J. Magn. Magn. Mater. **560**, 169596 (2022).

[20] J. H. Mentink, J. Hellsvik, D. V. Afanasiev, B. A. Ivanov, A. Kirilyuk, A. V. Kimel, O. Eriksson, M. I. Katsnelson, and T. Rasing, Ultrafast spin dynamics in multisublattice magnets, Phys. Rev. Lett. **108**, 057202 (2012).

[21] F. Jakobs and U. Atxitia, Atomistic spin model of single pulse toggle switching in Mn_2Ru_xGa Heusler alloys, Appl. Phys. Lett. **120**, 172401 (2022).

[22] R. F. L. Evans, W. J. Fan, P. Chureemart, T. A. Ostler, M. O. A. Ellis and R. W. Chantrell, Atomistic spin model simulations of magnetic nanomaterials, J. Phys.: Condens. Matter **26**, 103202 (2014).

[23] U. Parlak, R. Adam, D. E. Bürgler, S. Gang, and C. M. Schneider, Optically induced magnetization reversal in $[Co/Pt]_N$ multilayers: Role of domain wall dynamics, Phys. Rev. B **98**, 214443 (2018).

[24] G. Kichin, M. Hehn, J. Gorchon, G. Malinowski, J. Hohlfeld, and S. Mangin, From multiple- to single-pulse all-optical helicity-dependent switching in ferromagnetic Co/Pt multilayers, Phys. Rev. Appl. **12**, 024019 (2019).

[25] S. Alebrand, A. Hassdenteufel, D. Steil, M. Cinchetti, and M. Aeschlimann, Interplay of heating and helicity in all-optical magnetization switching, Phys. Rev. B **85**, 092401 (2012).

[26] S. Wurmehl, H. C. Kandpal, G. H. Fecher, and C. Felser, Valence electron rules for prediction of half-metallic compensated-ferrimagnet behaviour of Heusler compounds with complete spin polarization, J. Phys.: Condens. Matter **18**, 6171 (2006).

[27] T. Graf, F. Casper, J. Winterlik, B. Balke, G. H. Fecher, and C. Felser, Crystal structure of new Heusler compounds, Z. Anorg. Allg. Chem. **635**, 976 (2009).

[28] K. Endo, T. Kanomata, H. Nishihara, and K. R. A. Ziebeck, Magnetic properties of new compounds $RuMn_2Sn$ and $RuMn_2Si$, J. Alloys Compd. **510**, 1 (2012).

[29] M. Hakimi, M. Venkatesan, K. Rode, K. Ackland, and J. M. D. Coey, The zero-magnetization Heusler ferrimagnet, J. Appl. Phys. **113**, 17B101 (2013).

[30] L. Wollmann, S. Chadov, J. Kübler, and C. Felser, Magnetism in cubic manganese-rich Heusler compounds, Phys. Rev. B **90**, 214420 (2014).

[31] L. Yang, B. Liu, F. Meng, H. Liu, H. Luo, E. Liu, W. Wang, and G. Wu, Magnetic properties of Heusler alloy Mn_2RuGe and Mn_2RuGa ribbons, J. Magn. Magn. Mater. **379**, 1 (2015).

[32] M. Žic, K. Rode, N. Thiyagarajah, Y.-C. Lau, D. Betto, J. M. D. Coey, S. Sanvito, K. J. O'Shea, C. A. Ferguson, D. A. MacLaren, and T. Archer, Designing a fully compensated half-metallic ferrimagnet, Phys. Rev. B **93**, 140202(R) (2016).

[33] G. Chang, S. Xu, H. Zheng, B. Singh, C. Hsu, G. Bian, N. Ali doust, I. Belopolski, D. S. Sanchez, S. Zhang, H. Lin, and M. Z.

Hasan, Room-temperature magnetic topological Weyl fermion and nodal line semimetal states in half-metallic Heusler Co_2TiX (X = Si, Ge, or Sn), Sci. Rep. **6**, 38839 (2016).

[34] Z. Wang, M. G. Vergniory, S. Kushwaha, M. Hirschberger, and E. V. Chulkov, Time-reversal-breaking Weyl fermions in magnetic Heusler alloys, Phys. Rev. Lett. **117**, 236401 (2016).

[35] J. Kübler and C. Felser, Weyl points in the ferromagnetic Heusler compound Co_2MnAl, Europhys. Lett. **114**, 47005 (2016).

[36] T. Song, Q. Ma, X.-W. Sun, Z.-J. Liu, X.-P. Wei, and J.-H. Tian, High-pressure and high-temperature physical properties of half-metallic full-Heusler alloy Mn_2RuSi by first-principles and quasi-harmonic Debye model, J. Magn. Magn. Mater. **424**, 359 (2017).

[37] W. Zhang, Y. Jin, R. Skomski, P. Kharel, X. Li, T. Chen, G. Zhao, D. Kim, S. Valloppilly, and D. J. Sellmyer, Mn_2CrGa-based Heusler alloys with low net moment and high spin polarization, J. Phys. D: Appl. Phys. **51**, 255001 (2018).

[38] B. Ernst, R. Sahoo, Y. Sun, J. Nayak, L. Müchler, A. K. Nayak, N. Kumar, J. Gayles, A. Markou, G. H. Fecher, and C. Felser, Anomalous Hall effect and the role of Berry curvature in Co_2TiSn Heusler films, Phys. Rev. B **100**, 054445 (2019).

[39] G. P. Zhang, Y. H. Bai, M. S. Si, and T. F. George, First-principles insight into all-optical spin switching in the half-metallic Heusler ferrimagnet Mn_2RuGa, Phys. Rev. B **105**, 054431 (2022).

[40] L. Wollmann, A. K. Nayak, S. S. P. Parkin, and C. Felser, Heusler 4.0: Tunable Materials, Annu. Rev. Mater. Res. **47**, 247 (2017).

[41] C. Banerjee, N. Teichert, K. Siewierska, Z. Gercsi, G. Atcheson, P. Stamenov, K. Rode, J. M. D. Coey, and J. Besbas, Single pulse all-optical toggle switching of magnetization without gadolinium in the ferrimagnet Mn_2Ru_xGa, Nat. Commun. **11**, 4444 (2020).

[42] G. P. Zhang, R. Meadows, A. Tamayo, Y. H. Bai, and T. F. George, An attempt to simulate laser-induced all-optical spin switching in a crystalline ferrimagnet, AIP Adv. **10**, 125323 (2020).

[43] F. Jakobs and U. Atxitia, Universal criteria for single femtosecond pulse ultrafast magnetization switching in ferrimagnets, Phys. Rev. Lett. **129**, 037203 (2022).

[44] G. P. Zhang, W. Hübner, G. Lefkidis, Y. Bai, and T. F. George, Paradigm of the time-resolved magneto-optical Kerr effect for femtosecond magnetism, Nat. Phys. **5**, 499 (2009).

[45] P. Blaha, K. Schwarz, G. K. H. Madsen, D. Kvasnicka, and J. Luitz, *WIEN2k, An Augmented Plane Wave+Local Orbitals Program for Calculating Crystal Properties* (Karlheinz Schwarz, Techn. Universität Wien, Austria, 2001).

[46] M. Murakami and G. P. Zhang, Strong ultrafast demagnetization due to the intraband transitions, J. Phys.: Condens. Matter **35**, 495803 (2023).

[47] See Supplemental Material at http://link.aps.org/supplemental/10.1103/PhysRevB.109.L220401 for containing additional information about our method, the underlying mechanism of AOS, numerical results of PB tensors, partial charges, and **k** convergence tests.

[48] P. N. Butcher and D. Cotter, *The Elements of Nonlinear Optics* (Cambridge University Press, Cambridge, 1990).

[49] R. R. Birss, *Symmetry and Magnetism* (North-Holland, Amsterdam, 1964).

[50] G. P. Zhang, M. S. Si, M. Murakami, Y. H. Bai, and T. F. George, Generating high-order optical and spin harmonics from ferromagnetic monolayers, Nat. Commun. **9**, 3031 (2018).

[51] M. Lax, *Symmetry Principles in Solid State and Molecular Physics* (John Wiley and Sons, New York, 1974).

[52] H. Regensburger, R. Vollmer, and J. Kirschner, Time-resolved magnetization-induced second-harmonic generation from the Ni(110) surface, Phys. Rev. B **61**, 14716 (2000).

[53] P. Scheid, J. Hohlfeld, G. Malinowski, A. Bergman, M. Hehn, W. Zhang, O. Eriksson, S. Lebgue, and S. Mangin, Uncovering the role of the light-induced reduction of the inter-atomic exchange in the ultrafast demagnetization of Fe, Co, and Ni, arXiv:2301.01055.

[54] S. Pancharatnam, Generalized theory of interference and its applications, Part I. Coherent pencils, Proc. Indian Acad. Sci. **44**, 247 (1956).

[55] M. V. Berry, Quantal phase factors accompanying adiabatic changes, Proc. R. Soc. London A **392**, 45 (1984).

[56] D. Vanderbilt, *Berry Phases in Electronic Structure Theory* (Cambridge University Press, Cambridge, 2018).

[57] G. Bonfiglio, K. Rode, G. Y. P. Atcheson, P. Stamenov, J. M. D. Coey, A. V. Kimel, Th. Rasing, and A. Kirilyuk, Sub-picosecond exchange-relaxation in the compensated ferrimagnet Mn_2Ru_xGa, J. Phys.: Condens. Matter **33**, 135804 (2021).

[58] W. Hübner and G. P. Zhang, Ultrafast spin dynamics in ferromagnetic nickel, Phys. Rev. B **58**, R5920 (1998).

[59] Y. Q. Liu, M. S. Si, and G. P. Zhang, Strong and nearly 100% spin-polarized second-harmonic generation from ferrimagnet Mn_2RuGa, Phys. Rev. A **108**, 033514 (2023).

[60] I. Galanakis, P. H. Dederichs, and N. Papanikolaou, Slater-Pauling behavior and origin of the half-metallicity of the full-Heusler alloys, Phys. Rev. B **66**, 174429 (2002).

[61] I. Galanakis, P. H. Dederichs, and N. Papanikolaou, Origin and properties of the gap in the half-ferromagnetic Heusler alloys, Phys. Rev. B **66**, 134428 (2002).

[62] A. K. Patel, Y. Venkateswara, S. S. Samatham, A. Lakhani, J. Nayak, K. G. Suresh, and A. Alam, Spin-valve nature and giant coercivity of a ferrimagnetic spin semimetal Mn_2IrGa, arXiv:2303.04649.

[63] T. Roy, M. Tsujikawa, and M. Shirai, *Ab initio* study of electronic and magnetic properties of Mn_2RuZ/MgO(001) heterojunctions (Z = Al, Ge), J. Phys.: Condens. Matter **33**, 145505 (2021). T. Roy, M. Tsujikawa and M. Shirai, Their earlier version also includes Z = Al, Ga, Si, Ge, see arXiv:2010.06761.

[64] G. P. Zhang, Y. H. Bai, and T. F. George, Switching ferromagnetic spins by an ultrafast laser pulse: Emergence of giant optical spin-orbit torque, Europhys. Lett. **115**, 57003 (2016).

[65] S. Abdelouahed and M. Alouani, Magnetic anisotropy in Gd, GdN, and $GdFe_2$ tuned by the energy of gadolinium $4f$ states, Phys. Rev. B **79**, 054406 (2009).

[66] S. C. Liebscher, M. K. Hagen, J. Hader, J. V. Moloney, and S. W. Koch, Microscopic theory for the incoherent resonant and coherent off-resonant optical response of tellurium, Phys. Rev. B **104**, 165201 (2021).

[67] M. K. Hagen, J. Hader, and J. V. Moloney, Symmetry-conserving treatment of the random-phase problem in nonlinear coherent optics modeling in solids, Phys. Rev. A **108**, 033510 (2023).